



Article

Detecting the Auroral Oval through CSES-01 Electric Field Measurements in the Ionosphere

Emanuele Papini ^{1,*} , Mirko Piersanti ^{1,2} , Giulia D'Angelo ¹ , Antonio Cicone ^{1,3} , Igor Bertello ¹ , Alexandra Parmentier ^{1,4} , Piero Diego ¹ , Pietro Ubertini ¹, Giuseppe Consolini ¹ and Zeren Zhima ⁵

¹ Istituto di Astrofisica e Planetologia Spaziali—INAF, Via del Fosso del Cavaliere, 00133 Rome, Italy

² Dipartimento di Scienze Fisiche e Chimiche, Università degli Studi Dell'Aquila, Via Vetoio, 67100 L'Aquila, Italy

³ Dipartimento di Ingegneria e Scienze dell'Informazione e Matematica, Università degli Studi Dell'Aquila, Via Vetoio, 67100 L'Aquila, Italy

⁴ Istituto Nazionale di Fisica Nucleare—Sezione di Roma “Tor Vergata”, Via della Ricerca Scientifica, 00133 Roma, Italy

⁵ National Institute of Natural Hazards, Ministry of Emergency Management of China, Beijing 100085, China

* Correspondence: emanuele.papini@inaf.it

Abstract: We present the results of a systematic study of the ionospheric electric field in the Auroral Oval (AO) region in the southern hemisphere. We exploit one year of electric field measurements taken by the Electric Field Detector (EFD) on board the Chinese Seismo-Electromagnetic Satellite-01 (CSES-01), flying at around 500 km altitude in a sun-synchronous orbit. We exploit the high temporal resolution of the EFD to devise a new technique for the detection of CSES-01 crossing of the AO using electric field measurements only. This new technique combines a Median-Weighted Local Variance Measure with Fast Iterative Filtering to automatically isolate high levels of electromagnetic activity caused by, e.g., particle precipitation and Field Aligned Currents (FACs) at auroral latitudes. We validate this new method against other standard proxies, such as the single-FAC product from the Swarm mission and the auroral radiance emission measured by the Special Sensor Ultraviolet Spectrographic Imager (SSUSI) units on board the Defense Meteorological Satellite Program (DMSP) constellation. Furthermore, we identify ~3000 orbits (out of a dataset of ~10,000) where CSES-01 crosses the AO boundary under conditions of high geomagnetic activity. This dataset represents the first step in the systematic study of the auroral electric field, with many potential applications to space weather, thanks to the large amount of continuous observations of the ionosphere by CSES-01 and the forthcoming CSES-02 mission.

Keywords: auroral ionosphere; electric field; ionosphere–magnetosphere coupling; detection algorithms



Citation: Papini, E.; Piersanti, M.; D'Angelo, G.; Cicone, A.; Bertello, I.; Parmentier, A.; Diego, P.; Ubertini, P.; Consolini, G.; Zhima, Z. Detecting the Auroral Oval through CSES-01 Electric Field Measurements in the Ionosphere. *Remote Sens.* **2023**, *15*, 1568. <https://doi.org/10.3390/rs15061568>

Academic Editors: Pavel Klimov and Boris Kozelov

Received: 30 January 2023

Revised: 6 March 2023

Accepted: 7 March 2023

Published: 13 March 2023



Copyright: © 2023 by the authors. Licensee MDPI, Basel, Switzerland. This article is an open access article distributed under the terms and conditions of the Creative Commons Attribution (CC BY) license (<https://creativecommons.org/licenses/by/4.0/>).

1. Introduction

The Earth's magnetosphere is a complex plasma environment surrounding our planet that is continuously disturbed by the solar wind and the overall solar activity (e.g., [1]). For instance, under extreme perturbed conditions, magnetic reconnection occurring at the sunward boundary of the magnetosphere enables the solar wind to inject mass, momentum, and energy into the magnetosphere and the ionosphere at high latitudes, triggering ionospheric responses (e.g., [2–4]). The subsequent reconfiguration of the magnetospheric–ionospheric system triggers geomagnetic storms and substorms that can disturb communications, damage spacecraft, and disrupt power grids, potentially affecting the daily activity of human societies (e.g., [5]).

Auroral latitudes are the crossroads of the magnetosphere–ionosphere dynamics. All current systems that connect the ionosphere to the outer magnetosphere, that is, the magnetosheath and the magnetotail, are routed to the Auroral Oval (AO) via the field lines of the geomagnetic field (e.g., [6]). The variability of these field-aligned currents (FACs) influences geomagnetic activity, and consequently the dynamics of the Earth's magnetospheric–

ionospheric field. For the above reasons, in situ electromagnetic field measurements of the AO, together with measurements of the ionospheric plasma, constitute an invaluable source of information for understanding geomagnetic activity and advancing our ability to forecast space weather events. For instance, pairs of FACs associated with Pulsating Auroras (PAs) have been detected during geomagnetic substorms by the Swarm spacecraft [7]. Because PAs are among the drivers of large variations of dB/dt in the midnight and post-midnight sectors [8], which in turn is a proxy for Geomagnetically Induced Currents (GICs), such measurements can further increase our GIC forecasting capabilities.

Detecting the time intervals at which a spacecraft flies inside the AO is not an easy task, as the size and position of the AO change continuously due to geomagnetic activity. Current methods use remote sensing of auroral activity by measuring auroral emission. This is achieved, for instance, by the Special Sensor Ultraviolet Spectrographic Imagers (SSUSI) on board the Defense Meteorological Satellite Program (DMSP) constellation [9]. However, the integration time of these instruments (on the order of one hour) is long compared to both the dynamic evolution of the AO and the typical flight time of an ionospheric spacecraft across it (only a few minutes). Moreover, the latitudinal coverage of remote auroral observations does not always include the orbit of the desired spacecraft.

Other methods developed for the detection of the AO exploit measurements of particle precipitation [10], the magnetogram inversion technique (MIT) [11], and the calculation of the standard deviation of the total electron content (TEC) derivative (i.e., the rate of the TEC index, or ROTI) [12]. Web services are available as well; these make use of a “virtual globe” [13] by collecting measurements from different sources. Again, these methods suffer from long integration times and/or partial temporal coverage. Therefore, a technique for in situ detection of AO crossings by space measurements would definitely be advantageous.

In this work, we introduce a new method for identifying events marked by high auroral activity directly from in situ electric field measurements of the high latitude ionosphere. Our method combines the Multivariate Fast Iterative Filtering (MvFIF, [14]) technique, a median weighted local variance measure (MWLVM), and a machine learning clustering algorithm to enable automatic detection of these events. We use data collected by the Electric Field Detector [15] on board CSES-01 [16]. The rest of this manuscript is organized as follows. In Section 2.1, we describe the data used for this study and introduce our new Auroral Oval Detection (AOD) method. The method is validated against SSUSI observations in Section 3. Finally, in Section 4 we show the results of the AOD method after application to one year of EFD observations and discuss its performance.

2. Materials and Methods

2.1. Data

For the present study, we use electric field measurements taken by the EFD on board CSES-01 in the Extremely Low Frequency (ELF) band [15,17]. The spacecraft moves along a sun-synchronous orbit at an altitude of ~ 500 km, i.e., inside the F2-layer of the ionosphere, and with an orbital period of ~ 94 min. Its inclination is 97.4° , with a 02:00 a.m. ascending-node local time and a revisit period of 5 days. Specifically, we use Level 2 ELF data, which provide vector electric field measurements taken continuously between roughly -65° and $+65^\circ$ of geographic latitude; for more details, see [16]. Beyond these latitudes, all CSES-01 payloads are switched off. Nevertheless, several orbits can be found along which CSES-01 flies across the AO, and even the polar cap, when satellite instruments remain switched on. This is due to both the tilt angle of the geomagnetic dipole and the variability of the geomagnetic activity, which causes the auroral regions to move toward lower geographic latitudes [18–20]. EFD data in the ELF band (hereafter, EFD-ELF data) are sampled at a frequency of 5 kHz, which corresponds to a sampling resolution of a few meters when taking into account the average spacecraft velocity (7.2 km/s).

We validate our detection algorithm against concurrent measurements of the auroral activity, namely, the auroral radiance emission (EDR-AUR data product) measured by SSUSI on board the DMSP-F17 satellite [9]. Further details on the data used are provided in the relevant sections of the manuscript.

2.2. Electric Field Properties in the Auroral Oval

In the auroral region, the electric field shows intermittent fluctuations with broadband spectra and distinct statistical properties with respect to lower latitudes. In particular, EFD measurements in the ELF band have been recently exploited by Consolini et al. (hereafter C21 [21]) to characterize the multiscale features generated in the electric field by particle precipitation and field-aligned currents (FACs) during periods of high geomagnetic activity. The different nature of electric field fluctuations in the AO is highlighted in Figure 1 (left panel), which shows the electric field measurements analyzed by C21 and taken from 21:40:29 UT to 21:49:52 UT on 11 August 2018; in the following, we refer to these measurements as the reference dataset. At that time, CSES-01 was flying from the southern polar cap towards the equator. Its trajectory is plotted as a red curve in the bottom right panel of Figure 1, superimposed on a coloured contour of the auroral radiance emission measured in the Lyman–Birge–Hopfield long (LBHL) band by the SSUSI instrumentation on board the DMSP-F17 satellite [9]. These measurements were taken from 20:55:09 UT to 22:36:38 UT on 11 August 2018. Superimposed on the auroral emission are the modeled equatorward and poleward boundaries of the AO (orange dashed curves) as obtained by fitting the GUVI global boundary model [22]. In the left panel of Figure 1, CSES-01 crossing of these boundaries is marked by vertical dashed orange lines, together with a fiducial error of $\pm 1.5^\circ$ (orange areas) which corresponds to the worst error in the fit (Larry Paxton, private communication). The presence of intense auroral activity is confirmed by almost concurrent Swarm observations of the same region; the L2-Single FAC product obtained from magnetic field measurements taken by Swarm A [23] (top right panel of Figure 1) clearly shows the presence of energetic FACs, as the amplitude of the measured current shows large fluctuations in the area between the AO boundaries.

To corroborate these data, in Figure 2 we show density measurements of ionized helium (He⁺, middle) and oxygen (O⁺, bottom) taken by the Plasma Analyzer Package (PAP) on board CSES-01 [24]. These measurements show an enrichment of He⁺ in the AO and lower polar cap. The presence of He⁺ is further evidence that CSES-01 was in a region of magnetic field lines connected to both the magnetosphere and to outer space, granted that ionospheric He⁺ can only be of solar origin. In the same figure, it is notable that a perturbation of the electric field amplitude (~ 0.1 V/m) (top panel, marked by a vertical red solid line) appears in correspondence with a peak in the He⁺ density (and a decrease in the O⁺ counterpart), which is consistent with the position of the equatorward AO boundary provided by the GUVI fit.

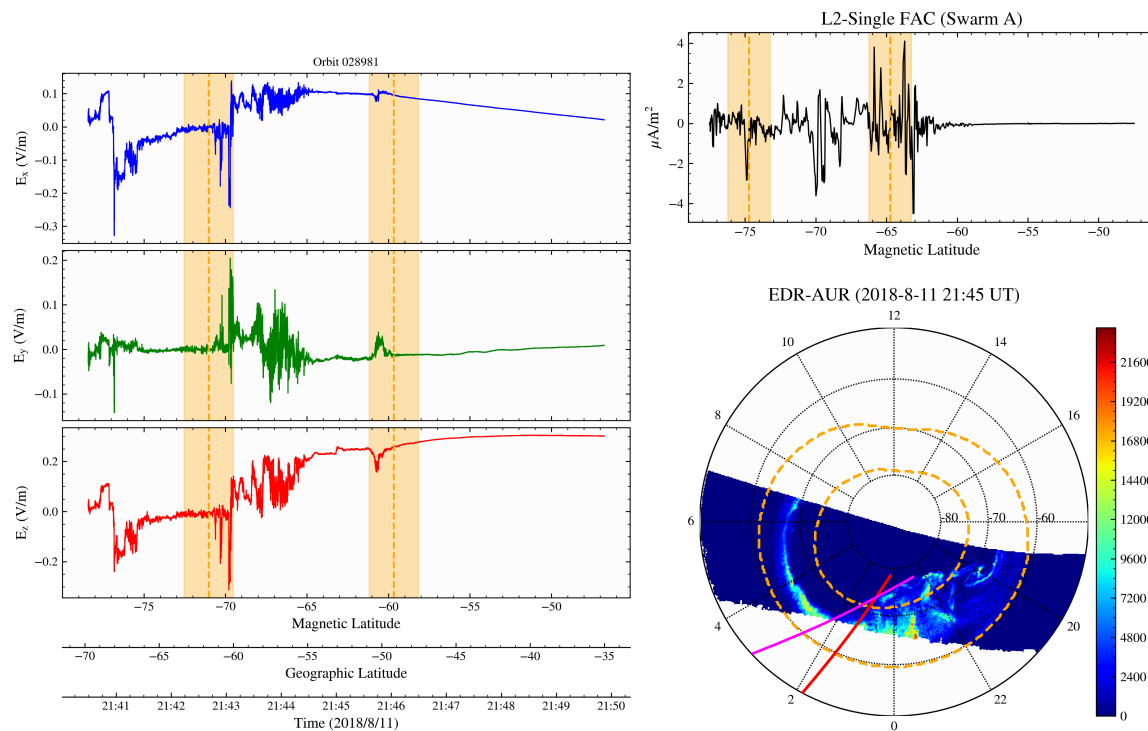


Figure 1. (Left): Electric field measurements collected by CSES-01/EFD on 11 August 2018 from 21:40:29 UT to 21:49:52 UT. The three components are in the spherical coordinates of the WGS84 reference frame. (Top right): L2-Single FAC product as calculated from Swarm A observations [23] taken on 11 August 2018 from 22:20:10 UT to 22:30:42 UT. (Bottom right): coloured contour of the auroral emission as measured in the LBHL band by the SSUSI instrument on board DMSP-F17 in the geomagnetic AACGM (Lat, MLT) reference frame. The orange dashed curves denote the modeled boundaries of the AO, the red curve is the orbital trajectory of CSES-01, and the magenta curve is the orbital trajectory of Swarm A, while the vertical dashed orange lines and areas in the left and top right panels denote the latitudes of the AO boundary from GUVI fits, together with a fiducial error of $\pm 1.5^\circ$.

2.3. Auroral Oval Detection Based on a Local Variance Measure of the Electric Field

Inside the AO and for the reference dataset (i.e., between $\sim -71^\circ$ and $\sim -60^\circ$ in magnetic latitude; see Figure 1), the variance of electric field fluctuations increases significantly, resulting in the electric energy being spread over several temporal/spatial scales. We identify this increase as the signature of the CSES-01 crossing of the AO. To automatically detect such a signature, we have developed a method that relies on Multivariate Fast Iterative Filtering (MvFIF) [14] to perform a multiscale decomposition of the vector electric field and that uses the Median Weighted Local Variance Measure (introduced here as a new measure, hereinafter MWLVM) to build a proxy of the auroral activity. MvFIF is designed to decompose a nonstationary nonlinear multivariate (i.e., vectorial) signal into a set of Intrinsic Mode Components (IMCs) oscillating around zero, with varying amplitude and frequency plus a residual or trend. After the proxy of the auroral activity has been calculated, a clustering algorithm is applied to identify the crossing of the AO by CSES-01. We refer to the overall procedure as the Auroral Oval Detection (AOD) algorithm.

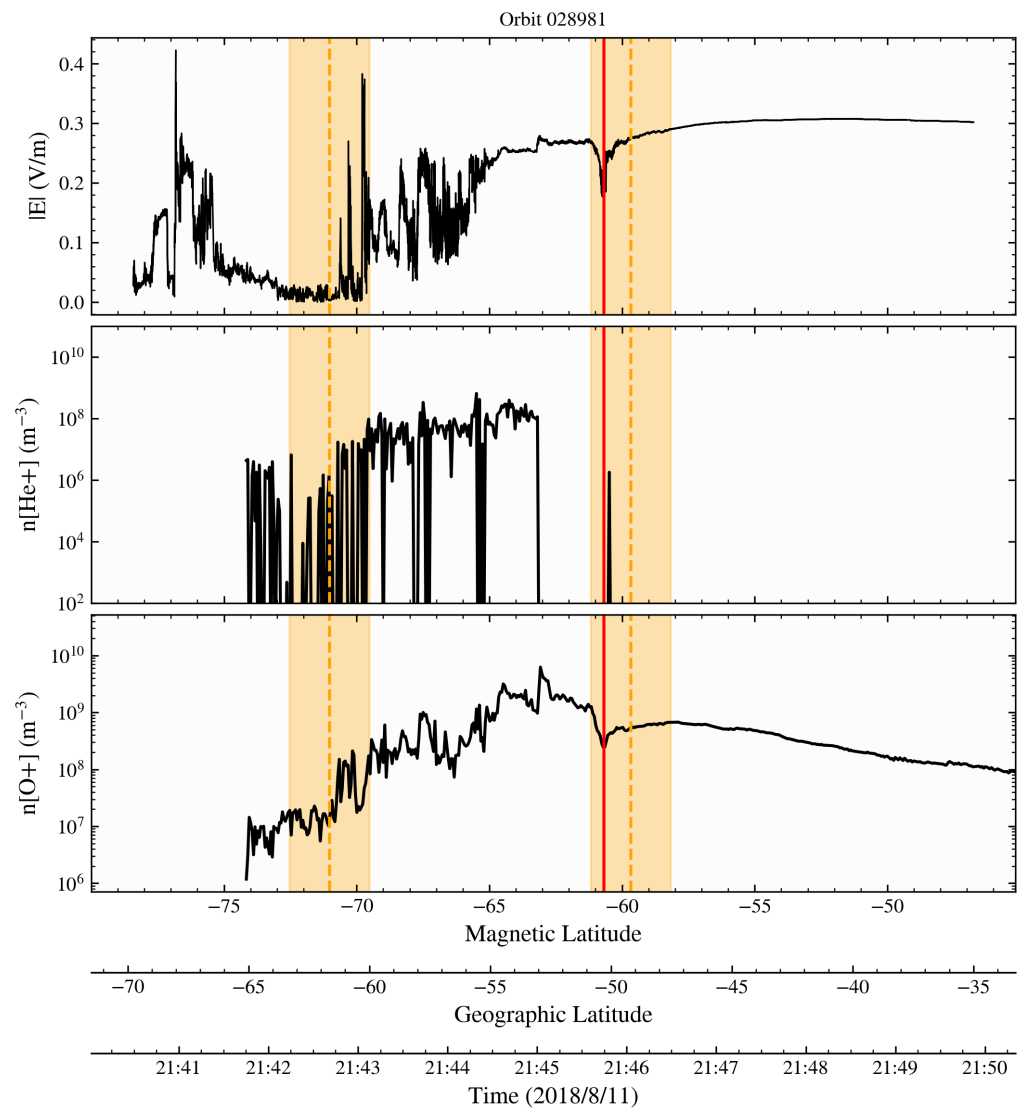


Figure 2. Electric field amplitude (top) and He⁺ (middle) and O⁺ (bottom) density as taken by PAP [24]. The vertical dashed orange lines and areas are the same as in the left panel of Figure 1.

We begin by taking EFD-ELF measurements of the vector electric field $E_{[xyz]}(t)$ in a time interval that corresponds to geographic latitudes above/below $\pm 35^\circ$, depending on whether we focus on the northern or the southern hemisphere. We then perform a MvFIF decomposition to obtain a set of Intrinsic Mode Components (IMC) $\hat{E}_{i,[xyz]}(t)$, such that

$$E_{[xyz]}(t) = \sum_{i=1}^M \hat{E}_{i,[xyz]}(t) + r_{[xyz]}(t), \quad (1)$$

where $r_{[xyz]}(t)$ is a residual that contains the largest-scale component of the electric field and M is the number of extracted IMCs. As an example, in Figure 3 we report the MvFIF decomposition of the y component of the electric field for the reference dataset (see Figure 1).

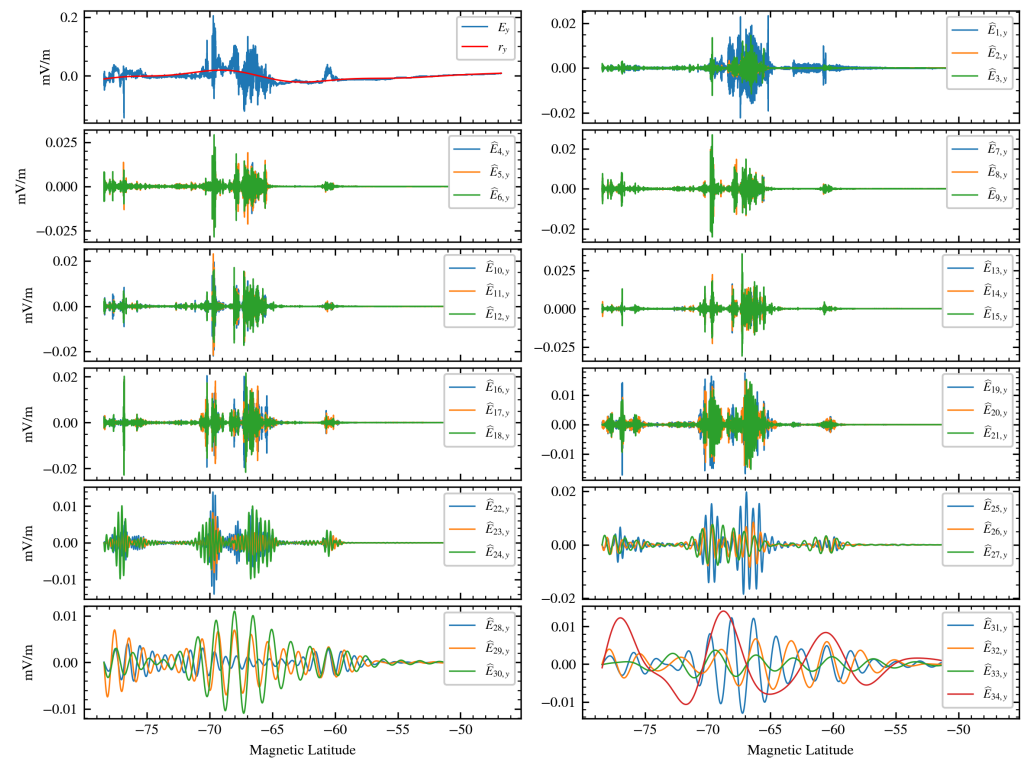


Figure 3. MvFIF decomposition, as introduced in Equation (1), of E_y measured by EFD in the selected interval (see Figure 1). (Top left): Original field component (blue curve) together with the residual r_y from the decomposition (red curve). The other panels show all the extracted IMCs. In total, 35 IMCs were found, from $\hat{E}_{1,y}$ to $\hat{E}_{35,y}$.

For each IMC, we take its moving variance $V_{i,[xyz]}(t, T_i)$

$$V_{i,[xyz]}(t, T_i) = \frac{1}{N} \sum_{\tau=t-T_i/2}^{t+T_i/2} \left(\hat{E}_{i,[xyz]}(\tau) - \mu_{i,[xyz]}(t, T_i) \right)^2 \quad (2)$$

Over a sliding window with length T_i corresponding to the size of the window function of the low-pass filter used by MvFIF to extract that same IMC. In the above equation, N is the number of sampling points contained in the interval T_i and

$$\mu_{i,[xyz]}(t, T_i) = \frac{1}{N} \sum_{\tau=t-T_i/2}^{t+T_i/2} \hat{E}_{i,[xyz]}(\tau) \quad (3)$$

Is the moving average of the i th IMC. The moving variance is then normalized to its median value over the whole time interval used for the analysis to obtain the MWLVM of the electric field:

$$V_{i,[xyz]}^{\text{med}}(t, T_i) = \frac{V_{i,[xyz]}(t, T_i)}{\text{med}\{V_{i,[xyz]}(t, T_i)\}_t}, \quad (4)$$

where $\text{med}\{\dots\}_t$ denotes the median operator. As defined, $V_{i,[xyz]}^{\text{med}}(t, T_i)$ measures the relative energy contained in the electric fluctuations at a given temporal scale T_i and time t . As an example, in the bottom panel of Figure 4 we show a contour plot of $V_{i,y}^{\text{med}}(t, T_i)$ as calculated from E_y (similar plots are obtained for the other two components). In this case, the MWLVM in the interval containing the AO (between -70° and -60° of magnetic latitude) increases at all frequencies above 1 Hz. This is expected, as the auroral electric field typically has a broadband energy distribution ([21] and references therein). To build the desired proxy, however, we further restrict the range of T_i to between 0.006 s and

0.03 s and between 0.2 s and 0.3 s (corresponding to two frequency bands between 33 Hz and 167 Hz and between 3.3 Hz and 5 Hz, respectively). These ranges have been chosen based on visual inspection of a few MWLVs from different orbits of CSES-01. This was done in order to avoid instrumental and ambient noise at high frequencies on the one hand, as well as spurious systematic signals introduced by instrument artifacts (typically found at around 10 Hz) on the other, allowing us to retain an accuracy of ~ 2 km (i.e., $\sim 0.017^\circ$ in latitude) in the detection of the AO signature (recall that the orbital speed of CSES-01 is ~ 7.2 km/s, for an accuracy of $\Delta x = 7.2 \text{ km/s} \cdot 0.3\text{s} \simeq 2 \text{ km}$, which corresponds to $\Delta \text{lat} = \Delta x / (R_E + h) \simeq 0.017^\circ$, where R_E is the Earth's radius and h is the altitude of CSES-01). Finally, we take

$$V_{[xyz]}^{\max}(t) = \max_{T_i \in \mathbb{A}} \{V_{i,[xyz]}^{\text{med}}(t, T_i)\}, \quad \mathbb{A} = [0.006\text{s}, 0.03\text{s}] \cup [0.2\text{s}, 0.3\text{s}]. \quad (5)$$

As our proxy for the auroral activity. In Figure 4 (middle panel), we show a plot of $V_y^{\max}(t)$ calculated from the electric field of the reference dataset.

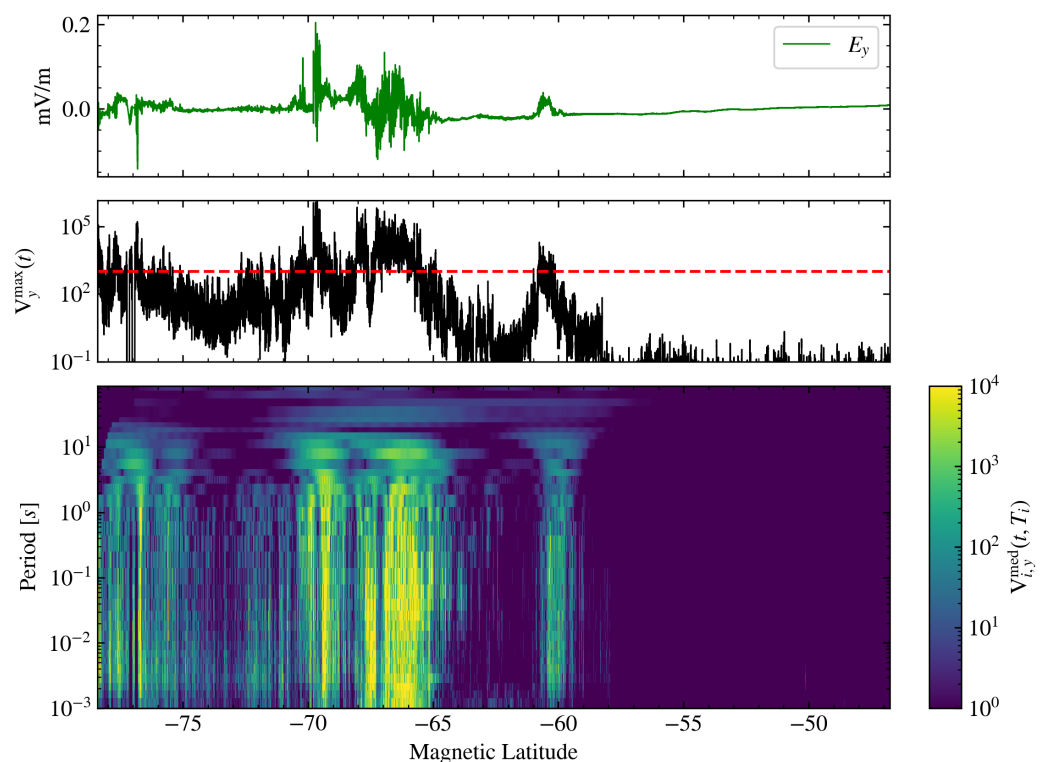


Figure 4. Coloured contour (**bottom panel**) of the Median Weighted Local Variance Measure $V_{i,y}^{\text{med}}(t, T_i)$ (see Equation (4)) of E_y (**top panel**) from the reference dataset. The proxy $V_y^{\max}(t)$ is shown in the (**middle panel**), together with the threshold of 1000 set for the clustering algorithm (see text for more details).

To detect the crossing of the AO, we apply a clustering algorithm (DBSCAN) to isolate the latitudinal/time intervals where $V_{[xyz]}^{\max}(t)$ exceeds a certain threshold, which we empirically set to 1000. To further reduce the probability of detecting false positives, we constrain such intervals to have a latitudinal extension of at least 1.5° and to not be in a time interval after/before 1 min and 15 s from/to the switching on/off of the spacecraft. In this way, we avoid spurious signals caused by the electronics; however, we include any detection with an interval that extends inside the on/off switching interval if its extension outside that interval exceeds 1.5° . In addition, we merge intervals that are separated by less than 0.5° of latitude. We stress that $V_{[xyz]}^{\max}$ is a relative measure (see Equation (2)); hence, the threshold of 1000 is relative with respect to the average variance present in the signal.

The clustering algorithm automatically adapts to the variance that is present in the signal considered. In other words, it is a differential measure of the auroral variance of the electric field with respect to the variance observed at low latitudes in the same orbit. The intervals returned by the clustering algorithm are identified as the intervals when the spacecraft crosses the AO region.

We note that although MvFIF decomposition is performed on the three components of the electric field concurrently, the subsequent detection procedure is applied to the same components separately. Therefore, the clustering algorithm may return different intervals (or no interval) depending on the component. We mark as a positive detection any occurrence when the clustering algorithm returns at least one interval detected in at least one of the electric field components. The northward and equatorward borders of the AO crossing are taken as the highest and lowest latitudinal borders detected for any of the three components. In Figure 5, we report the results obtained by applying the AOD algorithm to the reference dataset. A positive detection has occurred inside the AO (marked by a semitransparent red area). The poleward boundary of the interval detected and identified as active is consistent with the poleward boundary obtained by the GUVI fits of the auroral radiance (green/red striped area). However, the equatorward boundary (the green area centered at roughly 60°) falls outside of the detected interval, despite a small interval above the detection threshold being present in the MWLVM proxy (see the bottom panel of Figure 5). This is a consequence of the 1.5° constraint on the latitudinal extension of the clusters. We further discuss this aspect in the last section of this work. Finally, we note that “quiet” intervals (in the sense of low MWLVM values) that fall inside the AO are obviously not detected by our AOD algorithm.

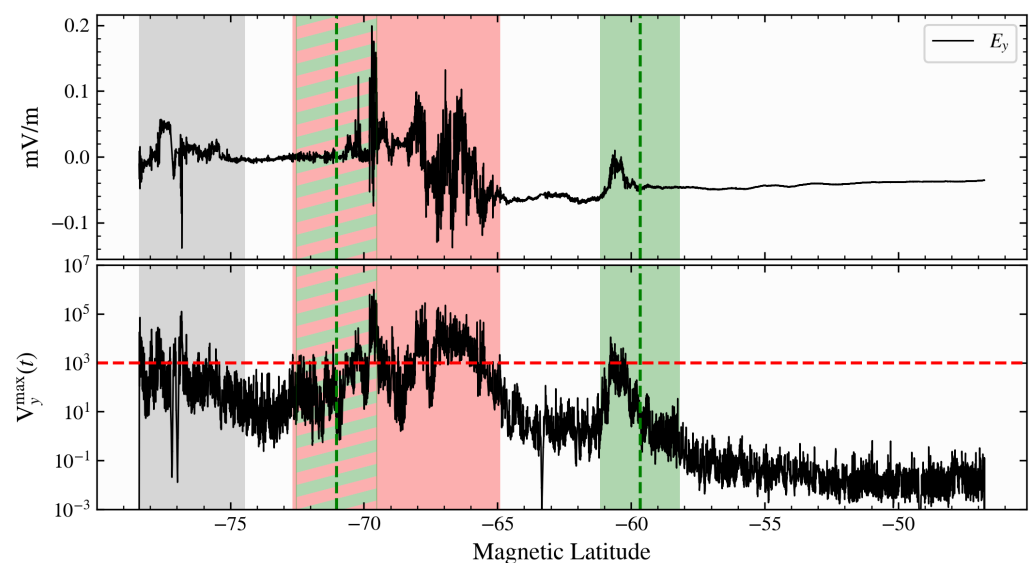


Figure 5. The y component of the electric field from the reference dataset (**top**) and proxy $V_y^{\max}(t)$ of the auroral activity (**bottom**). The horizontal red dashed line denotes the threshold of 1000 set for the clustering detection algorithm. The red area denotes the interval of high auroral activity detected by the clustering algorithm. The gray area denotes the part of the timeseries excluded from the analysis because it is potentially affected by the on/off switching of the instrument. Vertical dashed green lines and green areas denote the latitude of the AO boundaries from GUVI fits (see Figure 1), while striped areas with mixed colors denote overlapping intervals.

3. Results

3.1. Numerical Implementation

The AOD algorithm introduced in the previous section was implemented in a data pipeline that allowed to automatically process all EFD-ELF data at our disposal. The pipeline was fully implemented in python, making use of just-in-time compilation (using numba) for

speed optimization. The MWLVM proxy was computed by means of a multithreaded fortran routine compiled using the f2py package. This is the most computationally demanding task. MvFIF decomposition was performed using a custom python package developed by our group; the package is available at <https://github.com/EmanuelePapini/FIF> (accessed on 11 September 2022). A flowchart highlighting the AOD algorithm is shown in Figure 6.

3.2. Validation of the Detection Algorithm

The AOD algorithm was validated starting from a few selected CSES-01 orbits to assess its performance in a variety of conditions encountered at auroral latitudes. These orbits were selected from a > 1 yr dataset, and are shown in Table 1. Validation was performed against SSUSI measurements of the auroral radiance and related GUVI fits of the AO boundaries. In the following, we separately discuss the performance of the algorithm in the southern and northern hemispheres.

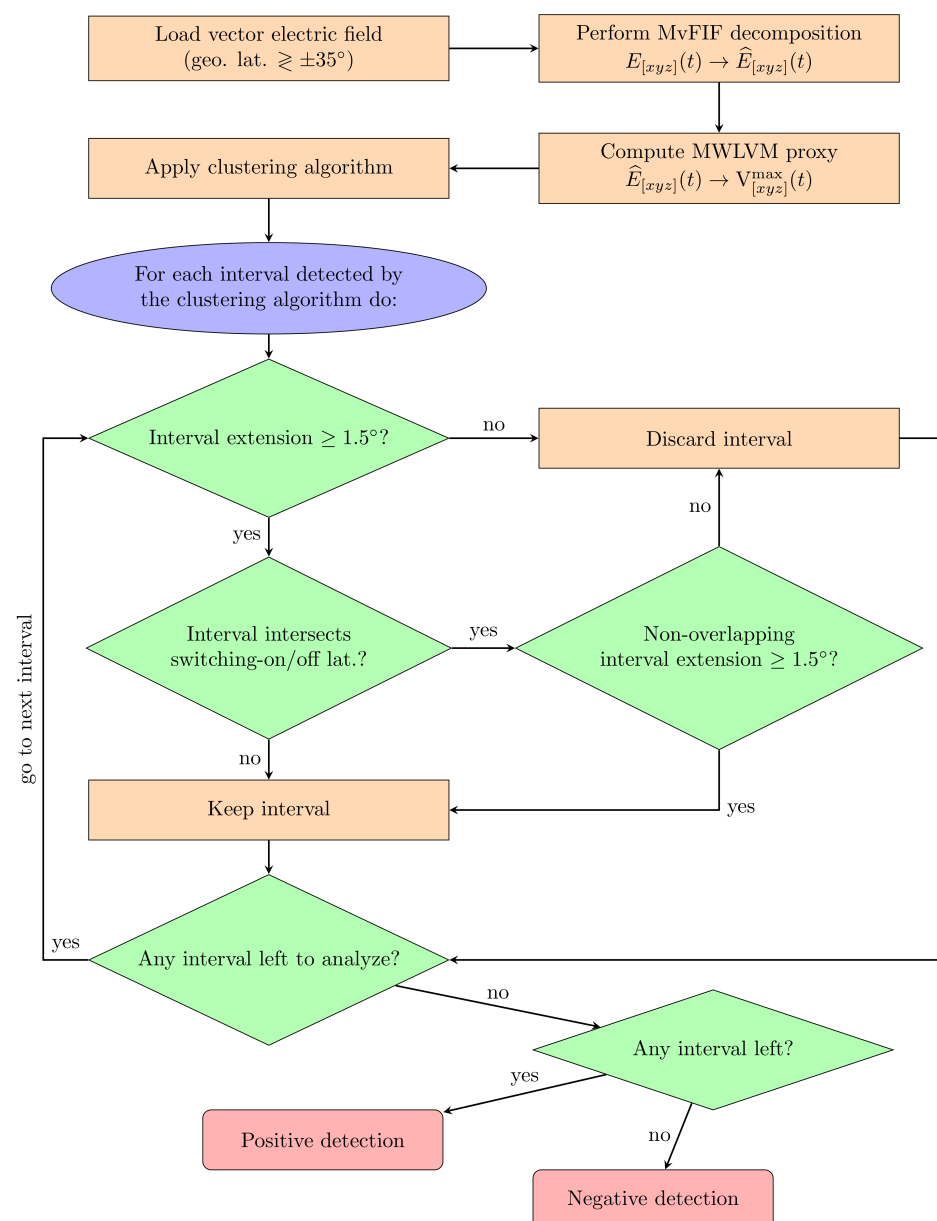


Figure 6. Flowchart describing the AOD algorithm.

Table 1. Table of the CSES-01 data shown in this work. The table reports, from left to right, the orbit number and the hemisphere (Northern [N] and Southern [S]), the side of the ionosphere analysed, the time interval considered for the analysis, the corresponding magnetic latitude (in AACGM coordinates), and the Kp and Ae indices (obtained from <https://www.spaceweatherlive.com/en/archive.html>, accessed on 21 September 2022, and <https://wdc.kugi.kyoto-u.ac.jp/aedir/>, accessed on 21 September 2022).

OrbitNum [N/S]	Side	UT Time Start ÷ End	Mag. Latitude Start/End (°)	Kp	Ae (nT)
2881 [S]	night	10 August 2018 18:49:57 ÷ 18:59:23	−84.61/−48.67	1	80
2888 [S]	night	11 August 2018 05:53:06 ÷ 06:02:32	−59.08/−30.35	2	220
2898 [N]	day	11 August 2018 20:53:04 ÷ 21:02:29	+78.83/+46.18	2	250
2898 [S]	night	11 August 2018 21:40:29 ÷ 21:49:54	−78.42/−46.78	4	550
2898 [N]	night	11 August 2018 22:08:21 ÷ 22:17:35	+33.88/+66.63	4	850
2912 [S]	night	12 August 2018 19:46:46 ÷ 19:56:13	−84.40/−48.55	2	100
3122 [N]	night	26 August 2018 15:49:09 ÷ 15:58:22	+31.81/+64.82	6	750
5060 [S]	day	1 January 2019 02:58:46 ÷ 03:06:51	−45.44/−77.18	1	<50
7243 [S]	night	24 May 2019 18:04:30 ÷ 18:12:37	−79.24/−48.50	2	50
8589 [S]	day	21 August 2019 07:01:23 ÷ 07:09:30	−48.59/−74.99	1	80
9095 [S]	night	23 August 2019 14:17:13 ÷ 14:25:18	−67.48/−42.67	1	<50

3.2.1. Southern Hemisphere

We begin with the results obtained from our analysis of observations taken on the night side. In Figure 7, we report a positive detection for orbit 7243. This orbit is geomagnetically quiet, as the AO has a small extension and a low auroral emission (see the right panel of Figure 7). In addition, both the Kp and the AE index are very low, with values of 2 and 50 nT, respectively. In this case, the AOD algorithm returns a positive detection consistent with the equatorward boundary of the AO (the red/green striped areas; striped areas with mixed colors denote overlapping intervals). The poleward boundary is not detected, as it partially falls inside the on/off switching interval (gray area). Figure 8 shows the results obtained for orbit 2888. In this case, the algorithm returns a negative detection. Again, this period is geomagnetically quiet; however, CSES-01 had its instruments switched off at a lower magnetic latitude than during orbit 7243.

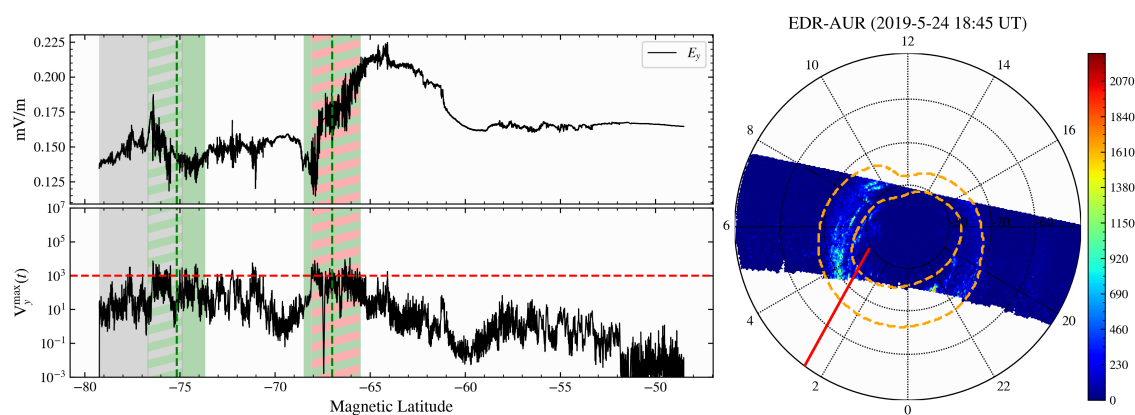


Figure 7. Same as Figure 5 (left) and the right panel of Figure 1 (right) except for orbit 7243. Positive detection, nightside southern hemisphere.

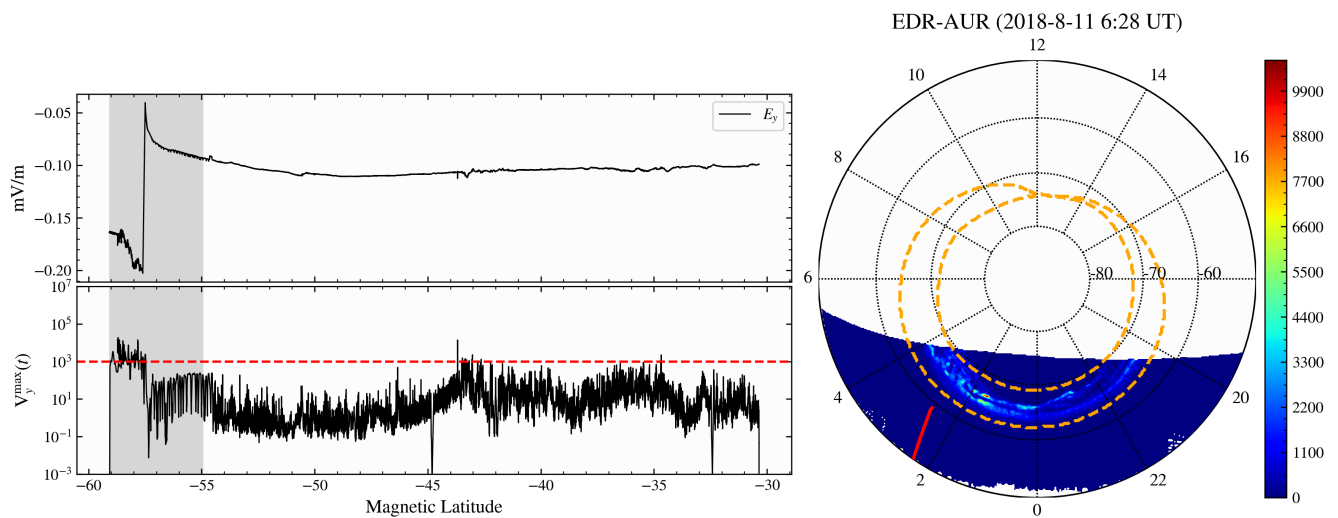


Figure 8. Same as Figure 7, except for orbit 2888. Negative detection, nightside southern hemisphere.

In Figure 9, we report what we labeled as a false positive detection on the night side of the southern hemisphere. In this case, the detection is at the limit of the on/off switching interval (the gray-shaded area). A distinct change in the electric field timeseries can be seen in its y component at $\sim -64.3^\circ$, likely caused by the switching on of the instrument. This is captured by our proxy V_y^{\max} , and because the detected cluster (red shaded area) extends more than 1.5° outside of the switching-on/off interval, it was marked as positive detection. According to SSUSI observations, however, CSES-01 did not cross the AO boundary. It may be argued that this could be a true positive detection based on the fact that the orbit was very close to the AO boundary as given by GUVI fits, and based on the fact that the latter are not a direct measure of the AO boundary.

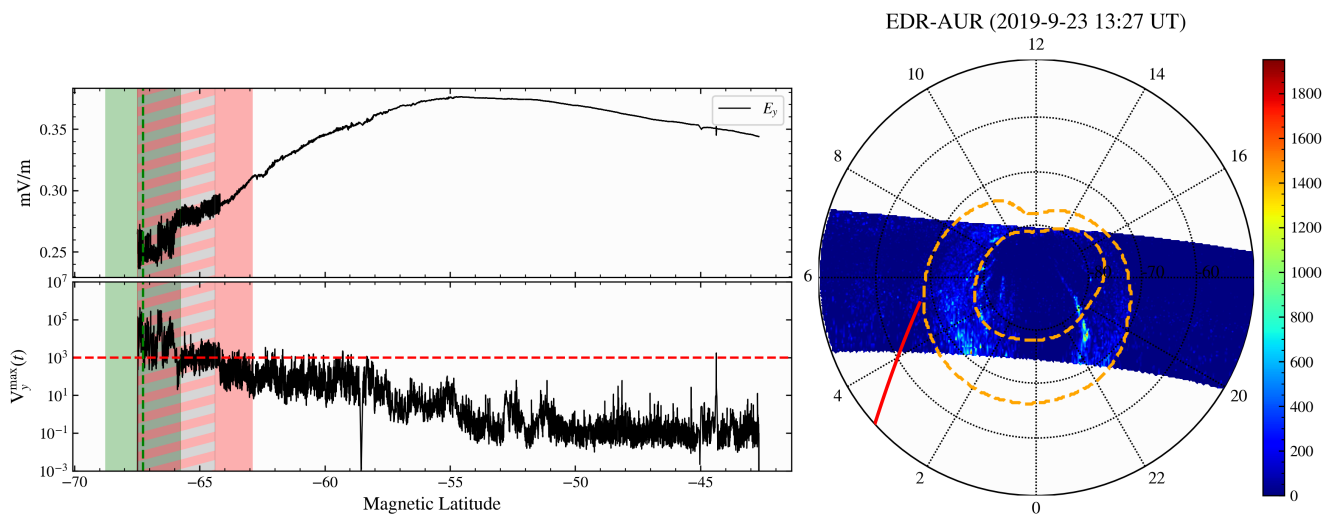


Figure 9. Same as Figure 7, except for orbit 9095. False Positive detection, nightside southern hemisphere.

Figure 10 reports an example of a correct negative detection on the dayside ionosphere. According to SSUSI, the spacecraft crossed the AO here only at the very end of the measurement window, well inside the on/off switching interval of the spacecraft. It is worth noting that negative detections are more common on the dayside, as the AO area is smaller.

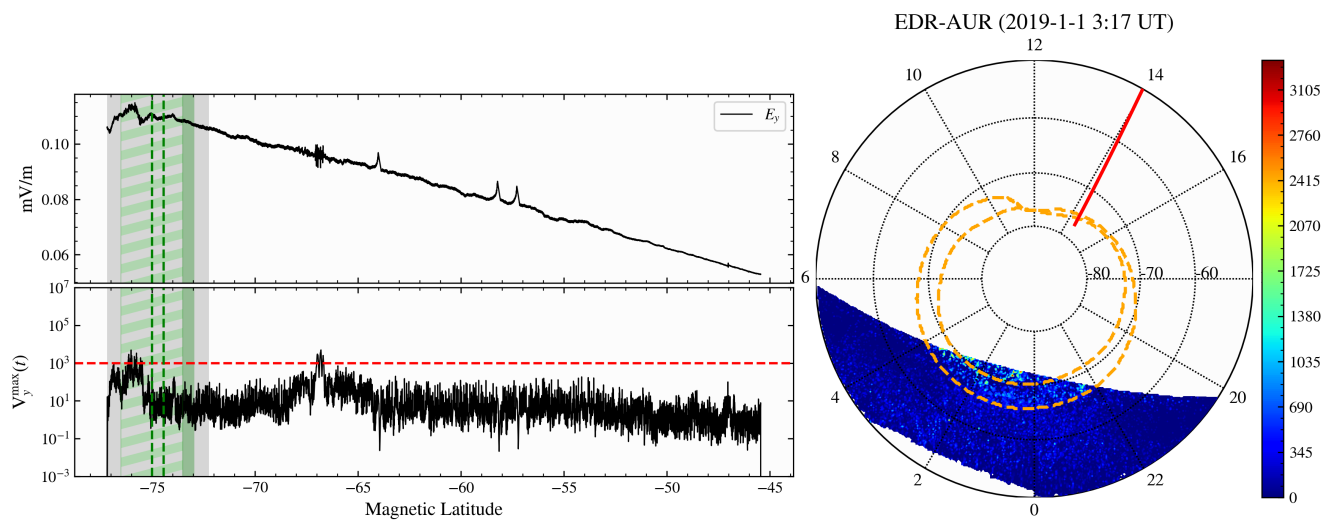


Figure 10. Same as Figure 7, except for orbit 5060. Negative detection, dayside southern hemisphere.

As a last example for the southern hemisphere, in Figure 11 we report another false positive detection on the dayside. Here, the AOD algorithm identifies an active interval between -66.8° and -68.6° magnetic latitude. It is indeed plausible that the real equatorward boundary of the AO is located at a lower latitude than the one given by GUVI fits. However, it is highly unlikely that the actual boundary is located at a much lower latitude.

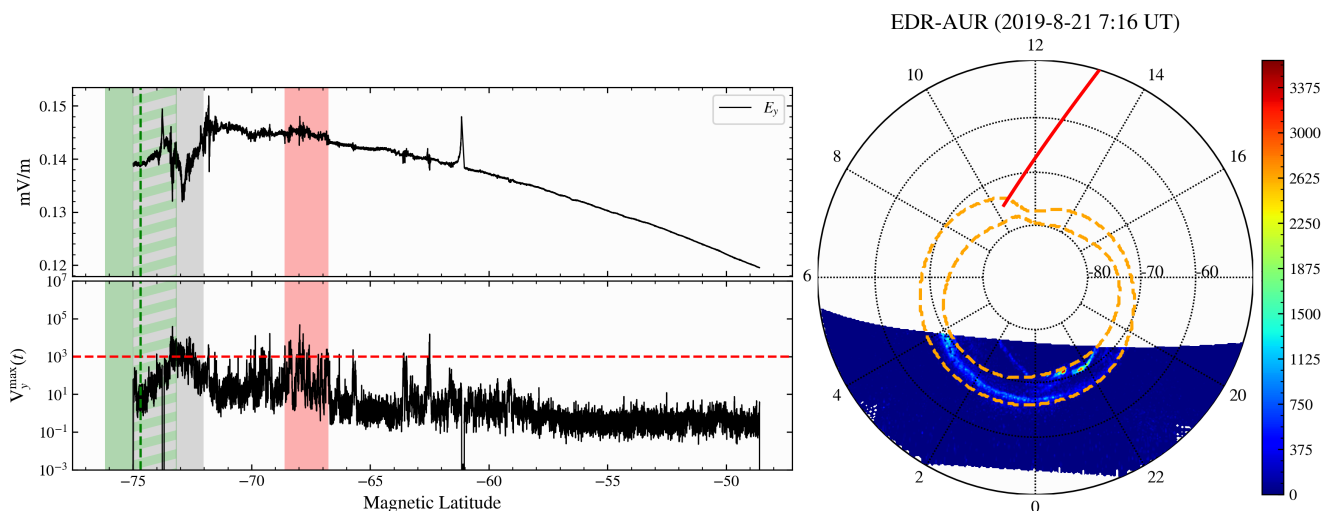


Figure 11. Same as Figure 7, except for orbit 8589. False Positive detection, dayside southern hemisphere.

3.2.2. Northern Hemisphere

In Figure 12, we report a dayside positive detection for orbit 2898 in the northern hemisphere. Here, the interval extension is small compared to the typical interval extension that can be found in the southern hemisphere. This is because in the northern hemisphere the AO is located at higher geographic latitudes. Thus, CSES-01 crossings of the AO with the EFD instrument switched on are less frequent and of smaller duration.

The next case we present is a false negative detection obtained on the night side during orbit 2898, and is shown in Figure 13. Here, the AOD algorithm returns no detection, although there is indeed a peak in V_y^{\max} that nicely matches the location of the equatorward AO boundary obtained from SSUSI. However, the latitudinal extension of this interval is less than 1.5° ; thus, our algorithm opts to discard it (see Figure 6).

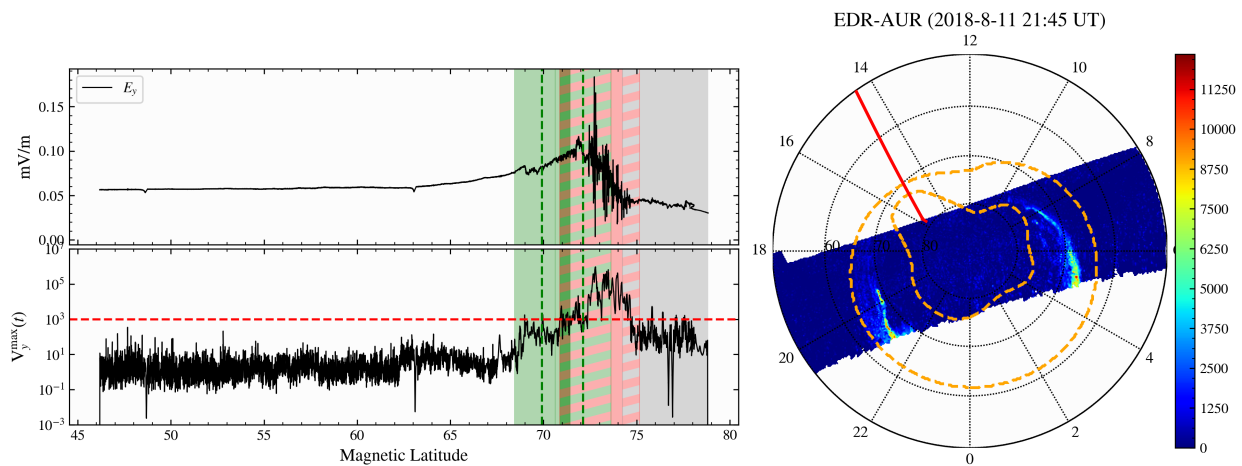


Figure 12. Same as Figure 7, except for orbit 2898. Positive detection, dayside Northern hemisphere.

As a last example, in Figure 14 we show another case in which the AOD algorithm returns a negative detection. In this case, no positive detection emerges because the activity is too low to reach the threshold for detection.

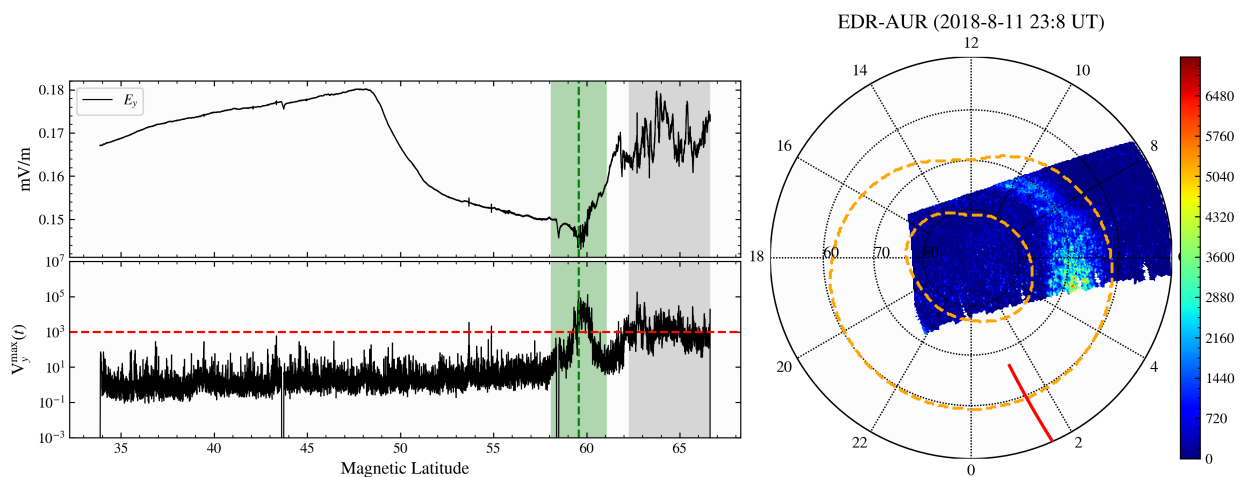


Figure 13. Same as Figure 7, except for orbit 2898. Negative detection, nightside northern Hemisphere. Crossing not detected because of short latitudinal interval (see text).

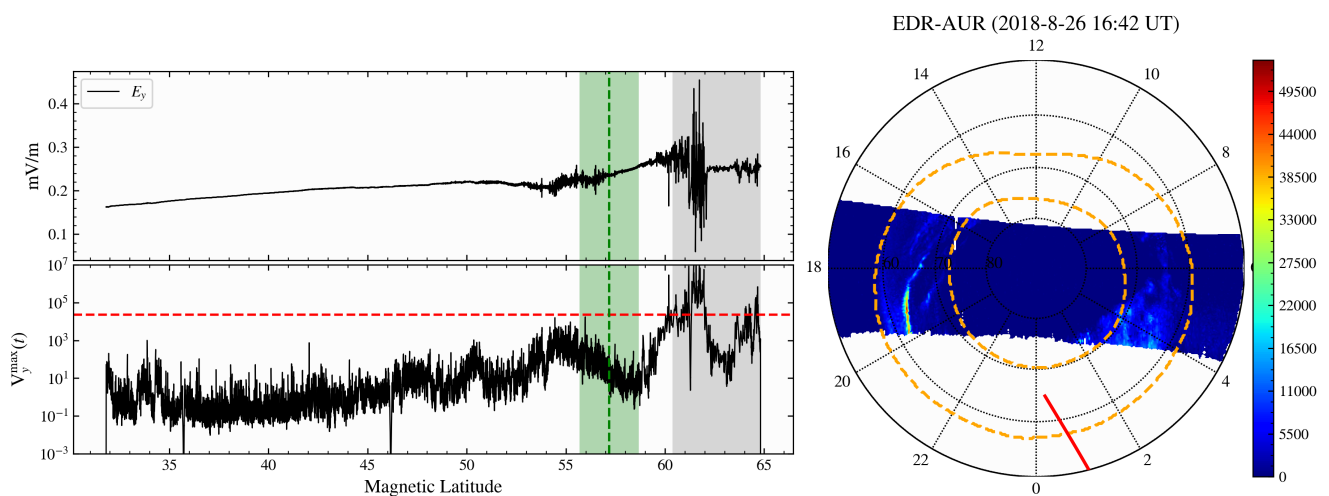


Figure 14. Same as Figure 7, except for orbit 3122. Negative detection, nightside northern hemisphere. Crossing not detected because of the threshold.

3.3. Polar Cap Detection

The final test cases we discuss are particularly interesting. The first one concerns a positive detection of activity in the polar cap. Figure 15 shows the results of AO detection on the night side of the southern hemisphere for orbit 2881. This is a geomagnetically quiet period characterized by low values of the Kp and AE index (1 and 80 nT, respectively). During this period, the AO has an almost regular shape and its latitudinal extension is small; see the right panel of Figure 15. At the same time, the AO is located at a relatively low geographic latitude, with the equatorward and poleward AO boundaries provided by SSUSI found at -65.7° and -70.9° magnetic latitude, corresponding to -51.2° and -56.2° geographic latitude, respectively. Therefore, EFD switches on while well inside the polar cap, at about -85° magnetic latitude. The AOD algorithm is able to detect the activity related to particle precipitation in the polar cap. Indeed, our proxy V_y^{\max} in the AO (the interval between the two dashed green lines) is low, and the very same electric field is “quiet”. Again, we note that while V^{\max} has a peak above the threshold at the equatorward boundary, its extension is very small; thus, the AOD algorithm discards the interval.

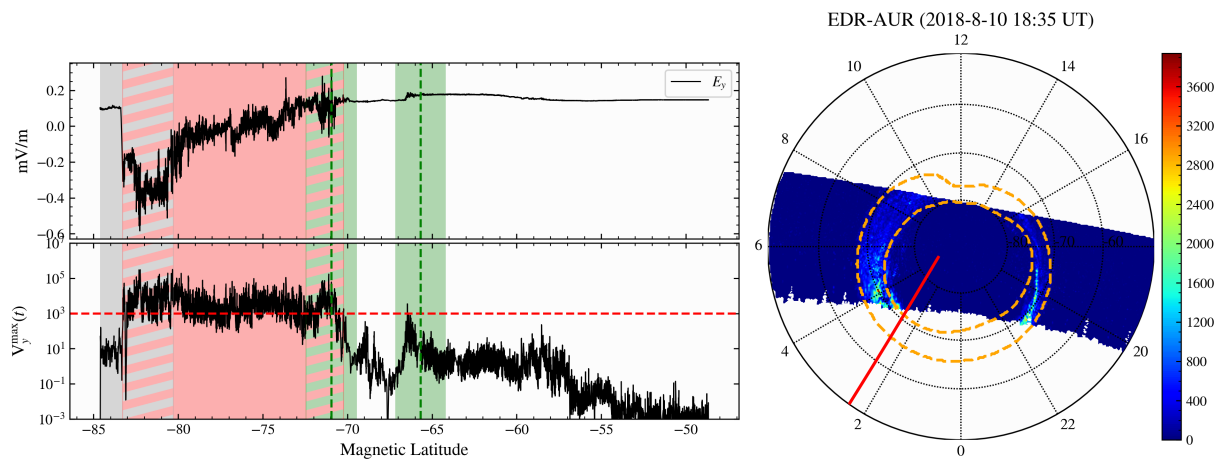


Figure 15. Same as Figure 8, except for orbit 2881. Positive detection of activity in the polar cap.

This detection turns out to be interesting when compared with another similar orbit in which the electric field in the polar cap is very quiet. This is the case of orbit 2912, shown in Figure 16. Here, the AOD algorithm correctly returns a positive detection in the AO near its northward boundary. It is worth noting that both the electric field and the MWLVM proxy for the two orbits are quantitatively similar, with similar values and trends at the same magnetic latitudes except in the polar cap.

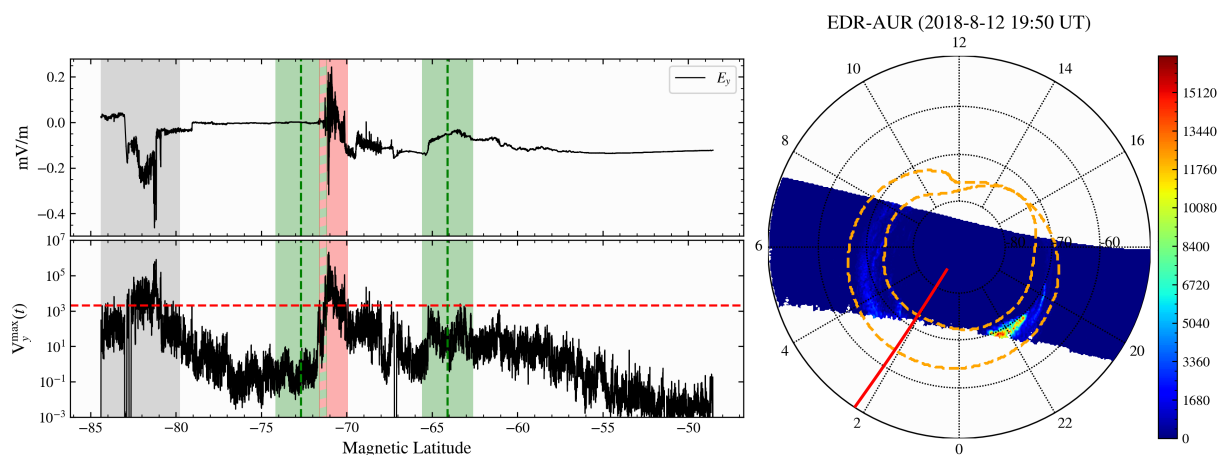


Figure 16. Same as Figure 8, except for orbit 2912. Positive detection of activity at the northward AO boundary with quiet interval in the polar cap.

4. Discussion

In this work, we have introduced a novel method for detecting CSES-01 crossings of the auroral oval during geomagnetically active periods. This has been achieved by means of in situ measurements of the ionospheric electric field and by identification of “active” intervals as those for which the relative energy of the electric field fluctuations at frequencies above ~ 3.3 Hz exceeds a given threshold with respect to its median values (calculated from measurements on the same orbit over all geographic latitudes above/below $\pm 35^\circ$). These intervals likely identify particle precipitation events in the high-latitude ionosphere.

The resulting AOD algorithm has been tested and validated against auroral radiance observations taken by the SSUSI spectrograph on board the DMSP-F17 satellite. A selection of the results from the validation campaign (shown in Section 3 and reported for convenience in Table 2) serves to highlight the ability of our algorithm in detecting active periods at auroral latitudes and to assess its limitations.

Table 2. AOD algorithm results for the validation samples analysed in this work. The table reports (from left to right) the orbit number and the hemisphere (Northern [N] and Southern [S]), the side of the ionosphere analysed, the outcome of the detection algorithm (true positive [TP] and true negative [TN] detection, false positive [FP] and false negative [FN] detection, and special positive [SP] detection), reason for wrong outcome, and the corresponding figure.

OrbitNum [N/S]	Side	AOD Result	Reason	Figure
2898 [S]	night	TP	-	Figure 5
7243 [S]	night	TP	-	Figure 7
2888 [S]	night	TN	-	Figure 8
9095 [S]	night	FP	spurious effects from electronics switching-on	Figure 9
5060 [S]	day	TN	-	Figure 10
8589 [S]	day	FP	activity interval detected at low latitudes	Figure 11
2898 [N]	day	TP	-	Figure 12
2898 [N]	night	FN	too short latitudinal interval of activity	Figure 13
3122 [N]	night	FN	too low activity levels	Figure 14
2881 [S]	night	SP	polar cap activity detected	Figure 15
2912 [S]	night	TP	positive detection with quiet polar cap	Figure 16

It is important to stress that cases of a false positive/false negative detection returned by the AOD algorithm are rare. Indeed, the validation campaign involved the analysis of about 50 orbits, and by visual inspection of the results we assessed that the AOD algorithm returned a correct answer (i.e., a true positive (TP) or a true negative (TN) detection) in more than 90% of cases. This confirms the ability of our new method to detect crossings of the AO during periods of high activity.

We stress that our method is designed to detect any physical process that manifests itself as an increase in the variance of the electric field fluctuations. Therefore, the algorithm detects regions of intense activity outside of the AO if present (e.g., the polar cap detection shown in Figure 15). Moreover, areas of moderate activity or of high activity with a small latitudinal extension are not detected. Considering several of the cases presented here (see Figures 5, 13, and 15), improvements in the detection of the AO boundary could be made by reducing the minimum latitudinal extension allowed before a cluster is discarded (see Figure 6). However, this would likely increase the number of false positive detections (see, e.g., the case of orbit 5060 shown in Figure 10, for which the cluster above the threshold at about -67° would be kept, resulting in a false positive). We note that positive detections are seemingly returned independently of the levels of geomagnetic activity provided by the AE and Kp indices. This is the case, for instance, for orbit 7243 (see Figure 7), where it is likely due to the chosen MWLVM proxy, which is weighted by the variance present in the signal for each particular orbit. This guarantees a certain level of independence in the method, as the proxy automatically calibrates itself based on the conditions below auroral latitudes.

Finally, the special case of detection over the polar cap (see Figures 15 and 16) deserves to be discussed. As already explained in Section 3.3, along orbits 2881 and 2912 CSES-01 flew for a considerable amount of time inside the southern polar cap region while taking measurements. For orbit 2912, the AOD algorithm correctly detects an active interval in the AO, while in the case of orbit 2881 it returns a positive detection in the polar cap due to the higher energy variance present there. Although the AOD algorithm was originally designed to detect activity in the AO, it is rather remarkable that it is capable of identifying and discerning such diverse conditions over the polar cap. Because we expect CSES-01 measurements of the polar cap to be taken once per day on average due to the misalignment of the magnetic dipole with respect to the rotation axis of the Earth, this opens up the possibility of using our AOD algorithm for studies of polar cap activity using CSES-01 data.

We conclude by reporting the results of running the AOD algorithm on the dataset of EFD-ELF measurements available for the year 2019 for the southern hemisphere, shown in Figure 17. This figure shows the histogram of positive and negative detections in blue and orange, respectively, grouped by month. In the same figure, we report the number of orbits that produced an error in the analysis, likely due to corrupted or misformatted data files. Out of 9808 orbits processed, 2784 positive detections were made, of which 65% returned a positive detection in each of the three components of the electric field, 17% in two components, and 18% in a single component. This dataset constitutes an invaluable basis for future investigations that aim to characterize the statistical properties of the electric field in the auroral oval, which we intend to address as a next step.

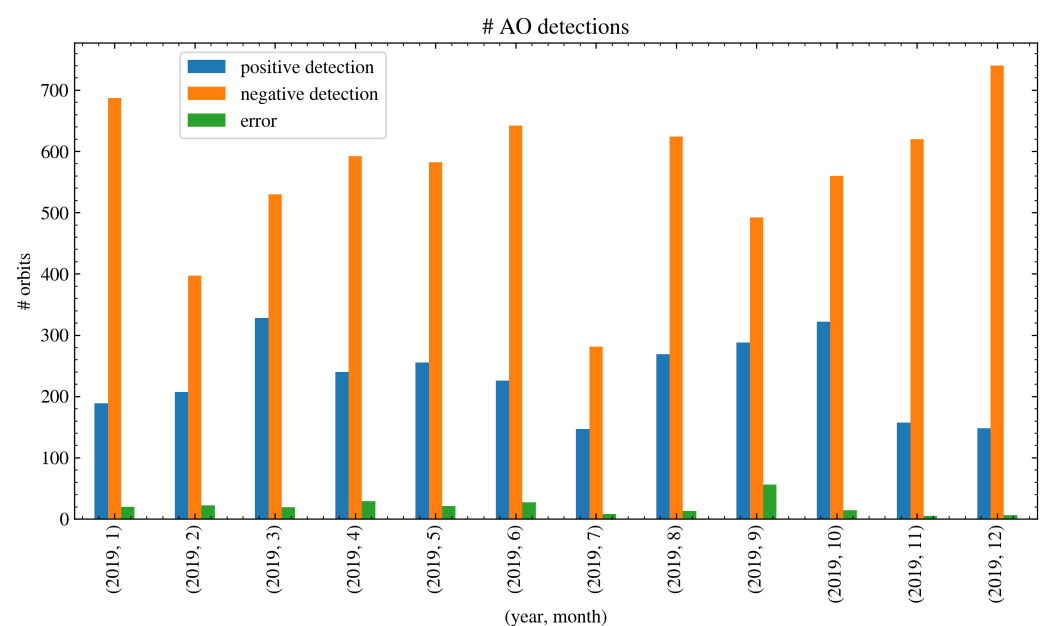


Figure 17. AO detection results in the southern hemisphere for CSES-01 orbits available in 2019. Blue and orange histograms denote positive and negative detection, respectively, while green histograms denote available orbits that could not be successfully analysed.

The results of this work represent the first step in the systematic study of the auroral electric field, with many potential applications in the framework of space weather thanks to the large amount of continuous ionospheric measurements carried out by CSES-01. The upcoming CSES-02 mission (scheduled for launch in late 2023) will provide continuous measurements over the entire latitudinal range, including the polar caps, holding the promise of further increasing our ability to probe electromagnetic fields in the ionosphere at all latitudes, and thereby advancing our understanding of the ionosphere–magnetosphere–solar wind couplings.

Author Contributions: Conceptualization, E.P., M.P., G.D., A.C., A.P., P.D., P.U. and G.C.; methodology, E.P., M.P. and A.C.; software, E.P. and A.C.; validation, E.P.; formal analysis, E.P.; investigation, E.P. and M.P.; resources, I.B., P.D., P.U. and Z.Z.; data curation, E.P., I.B., Z.Z. and M.P.; writing—original draft preparation, E.P.; writing—review and editing, E.P., M.P., G.D., A.C., I.B., A.P., P.D., P.U., G.C. and Z.Z.; visualization, E.P.; project administration, M.P. and P.D.; funding acquisition, P.D. and P.U. All authors have read and agreed to the published version of the manuscript.

Funding: This research received financial support from the Italian Space Agency under the contract ASI “LIMADOU Scienza+” No. 2020-31-HH.0.

Data Availability Statement: The original EFD data taken by CSES-01 are available at <http://www.leos.ac.cn/#/home> (accessed on 11 November 2020). SSUSI EDR-AUR data products used in this work are publicly available at https://ssusi.jhuapl.edu/data_products (accessed on 16 September 2022).

Acknowledgments: This work made use of data from the CSES-01 mission, a project funded by the China National Space Administration and the China Earthquake Administration in collaboration with the Italian Space Agency and the Istituto Nazionale di Fisica Nucleare. M. Piersanti and G. D’Angelo thank the ISSI-BJ project “electromagnetic data validation and scientific application research based on CSES satellite” and Dragon 5 cooperation 2020–2024 (ID. 59236). E. Papini wishes to thank Larry Paxton for providing information on SSUSI data products. A. Cicone is a member of the Italian “Gruppo Nazionale di Calcolo Scientifico” (GNCS) of the Istituto Nazionale di Alta Matematica “Francesco Severi” (INdAM).

Conflicts of Interest: The authors declare no conflict of interest. The funders had no role in the design of the study; in the collection, analyses, or interpretation of data; in the writing of the manuscript, or in the decision to publish the results.

References

1. Borovsky, J.E.; Valdivia, J.A. The Earth’s Magnetosphere: A Systems Science Overview and Assessment. *Surv. Geophys.* **2018**, *39*, 817–859. [\[CrossRef\]](#) [\[PubMed\]](#)
2. D’Angelo, G.; Piersanti, M.; Alfonsi, L.; Spogli, L.; Clausen, L.B.N.; Coco, I.; Li, G.; Baiqi, N. The response of high latitude ionosphere to the 2015 St. Patrick’s day storm from in situ and ground based observations. *Adv. Space Res.* **2018**, *62*, 638–650. [\[CrossRef\]](#)
3. D’Angelo, G.; Piersanti, M.; Alfonsi, L.; Spogli, L.; Coco, I.; Li, G.; Baiqi, N. The response of high latitude ionosphere to the 2015 June 22 storm. *Ann. Geophys.* **2019**, *62*. [\[CrossRef\]](#)
4. D’Angelo, G.; Piersanti, M.; Pignalberi, A.; Coco, I.; De Michelis, P.; Tozzi, R.; Pezzopane, M.; Alfonsi, L.; Cilliers, P.; Ubertini, P. Investigation of the Physical Processes Involved in GNSS Amplitude Scintillations at High Latitude: A Case Study. *Remote Sens.* **2021**, *13*, 2493. [\[CrossRef\]](#)
5. Eastwood, J.P.; Nakamura, R.; Turc, L.; Mejnertsen, L.; Hesse, M. The Scientific Foundations of Forecasting Magnetospheric Space Weather. *Space Sci. Rev.* **2017**, *212*, 1221–1252. [\[CrossRef\]](#)
6. Ganushkina, N.Y.; Liemohn, M.W.; Dubyagin, S. Current Systems in the Earth’s Magnetosphere. *Rev. Geophys.* **2018**, *56*, 309–332. [\[CrossRef\]](#)
7. Gillies, D.M.; Knudsen, D.; Spanswick, E.; Donovan, E.; Burchill, J.; Patrick, M. Swarm observations of field-aligned currents associated with pulsating auroral patches. *J. Geophys. Res.* **2015**, *120*, 9484–9499. [\[CrossRef\]](#)
8. Zou, Y.; Dowell, C.; Ferdousi, B.; Lyons, L.R.; Liu, J. Auroral Drivers of Large dB/dt During Geomagnetic Storms. *Space Weather* **2022**, *20*, e2022SW003121. [\[CrossRef\]](#)
9. Paxton, L.J.; Meng, C.I.; Fountain, G.H.; Ogorzalek, B.S.; Darlington, E.H.; Gary, S.A.; Goldsten, J.O.; Kusnierkiewicz, D.Y.; Lee, S.C.; Linstrom, L.A.; et al. SSUSI: Horizon-to-horizon and limb-viewing spectrographic imager for remote sensing of environmental parameters. In *Proceedings of the Ultraviolet Technology IV, San Diego, CA, USA, 20–21 July 1992*; Society of Photo-Optical Instrumentation Engineers (SPIE) Conference Series; Huffman, R.E., Ed.; SPIE: Washington, DC, USA, 1993; Volume 1764, pp. 161–176. [\[CrossRef\]](#)
10. Newell, P.T.; Feldstein, Y.I.; Galperin, Y.I.; Meng, C.I. Morphology of nightside precipitation. *J. Geophys. Res.* **1996**, *101*, 10737–10748. [\[CrossRef\]](#)
11. Lunyushkin, S.; Pensikh, Y. Diagnostics of auroral oval boundaries on the basis of the magnetogram inversion technique. *Sol.-Terr. Phys.* **2019**, *5*, 88–100. [\[CrossRef\]](#)
12. Edemskiy, I.K.; Yasyukevich, Y.V. Auroral Oval Boundary Dynamics on the Nature of Geomagnetic Storm. *Remote Sens.* **2022**, *14*, 5486. [\[CrossRef\]](#)
13. Vorobev, A.; Pilipenko, V.; Krasnoperov, R.I.; Vorobeva, G.; Lorentzen, D.A. Short-term forecast of the auroral oval position on the basis of the “virtual globe” technology. *Russ. J. Earth. Sci.* **2020**, *20*, ES5007. [\[CrossRef\]](#)
14. Cicone, A.; Pellegrino, E. Multivariate Fast Iterative Filtering for the Decomposition of Nonstationary Signals. *IEEE Trans. Signal Process.* **2022**, *70*, 1521–1531. [\[CrossRef\]](#)

15. Huang, J.; Lei, J.; Li, S.; Zeren, Z.; Li, C.; Zhu, X.; Yu, W. The Electric Field Detector (EFD) onboard the ZH-1 satellite and first observational results. *Earth Planet. Phys.* **2018**, *2*, 469–478. [[CrossRef](#)]
16. Shen, X.; Zhang, X.; Yuan, S.; Wang, L.; Cao, J.; Huang, J.; Zhu, X.; Piergiorgio, P.; Dai, J. The state-of-the-art of the China Seismo-Electromagnetic Satellite mission. *Sci. China E: Technol. Sci.* **2018**, *61*, 634–642. [[CrossRef](#)]
17. Diego, P.; Huang, J.; Piersanti, M.; Badoni, D.; Zeren, Z.; Yan, R.; Rebustini, G.; Ammendola, R.; Candidi, M.; Guan, Y.B.; et al. The Electric Field Detector on Board the China Seismo Electromagnetic Satellite—In-Orbit Results and Validation. *Instruments* **2021**, *5*, 1. [[CrossRef](#)]
18. Feldstein, Y.I. Auroral morphology, II. Auroral and geomagnetic disturbances. *Tellus* **1964**, *16*, 252–257. [[CrossRef](#)]
19. Vorobjev, V.G.; Yagodkina, O.I. Seasonal and UT variations of the position of the auroral precipitation and polar cap boundaries. *Geomagn. Aeron.* **2010**, *50*, 597–605. [[CrossRef](#)]
20. Wagner, D.; Neuhauser, R. Variation of the auroral oval size and offset for different magnetic activity levels described by the Kp-index. *Astron. Nachrichten* **2019**, *340*, 483–493. [[CrossRef](#)]
21. Consolini, G.; Quattrocioni, V.; D’Angelo, G.; Alberti, T.; Piersanti, M.; Marcucci, M.F.; De Michelis, P. Electric Field Multifractal Features in the High-Latitude Ionosphere: CSES-01 Observations. *Atmosphere* **2021**, *12*, 646. [[CrossRef](#)]
22. Zhang, Y.; Paxton, L.J. An empirical Kp-dependent global auroral model based on TIMED/GUVI FUV data. *J. Atmos. Sol.-Terr. Phys.* **2008**, *70*, 1231–1242. [[CrossRef](#)]
23. Ritter, P.; Lühr, H.; Rauberg, J. Determining field-aligned currents with the Swarm constellation mission. *Earth, Planets Space* **2013**, *65*, 1285–1294. [[CrossRef](#)]
24. Liu, C.; Guan, Y.; Zheng, X.; Zhang, A.; Piero, D.; Sun, Y. The technology of space plasma in-situ measurement on the China Seismo-Electromagnetic Satellite. *Sci. China E: Technol. Sci.* **2019**, *62*, 829–838. [[CrossRef](#)]

Disclaimer/Publisher’s Note: The statements, opinions and data contained in all publications are solely those of the individual author(s) and contributor(s) and not of MDPI and/or the editor(s). MDPI and/or the editor(s) disclaim responsibility for any injury to people or property resulting from any ideas, methods, instructions or products referred to in the content.